

Revealing intricate acto-myosin dynamics at a membrane surface using interferometric scattering microscopy

Darius Köster^{1,2,*}, Nikolas Hundt³, Gavin Young³, Adam Fineberg³, Philipp Kukura³, Satyajit Mayor^{1,4}

1 National Centre for Biological Sciences, Tata Institute for Fundamental Research, GKVK, Bellary Road, Bangalore, 560065, India

2 Division of Biomedical Sciences, Warwick Medical School, University of Warwick, Coventry CV4 7AL, UK

3 Physical and Theoretical Chemistry Laboratory, Department of Chemistry, University of Oxford, South Parks Road, Oxford OX1 3QZ, UK

4 Institute for Stem Cell Biology and Regenerative Medicine, Bangalore 560065, India

* corresponding author: d.koester@warwick.ac.uk

Abstract

The surface of mammalian cells, i.e. the plasma membrane and the underlying cytoskeletal cortex, constitutes an active platform for many cellular processes including cargo uptake, signaling and formation of cell adhesions. Experimental and theoretical work has recently shown that acto-myosin dynamics can modify the local membrane organization, but the molecular details are not well understood. Here, we demonstrate the potential of iSCAT microscopy, a label free imaging technique, to interrogate single molecule processes in the context of mesoscale dynamics. In a minimal acto-myosin network linked to supported lipid bilayers, we measure single actin and myosin II filament dynamics as well as whole network flow and organization. We show that the binding kinetics and processivity of myosin II filaments vary with the ATP concentration and identify a regime that promotes whole network contractility. This combination of techniques provides an ideal tool to bridge multiple length scales ranging from single myosin head binding kinetics up to network contraction on the mesoscopic scale, and we believe that this approach will be useful for the investigations of multi-component systems.

Introduction

The acto-myosin cortex in living cells is necessary for the mechanical stability of the cell and influences the organization of the adjacent plasma membrane. Several studies have shown that the cell cortex influences the dynamics and mobility of particular membrane components (1–3) and there is increasing evidence that the dynamic remodeling of the acto-myosin network drives the local concentration and clustering of membrane molecules (4–7). The complexity of the acto-myosin cortex and the plasma membrane in live cells makes it difficult to study the molecular details of cortex-membrane interactions and to uncover the underlying mechanisms.

Reconstituted minimal systems provide a tractable way to studying the dynamics of a two-dimensional, membrane bound acto-myosin network, in which fluorescently labeled proteins are dynamically visualized using confocal or TIRF (total internal reflection fluorescence) microscopy (8–11). To capture the full dynamics of the acto-myosin network and to span the temporal range from fast single molecule interactions to long-term network deformations, it is necessary to visualize the network components with a sub-second time-resolution over timescales of tens of minutes. This is difficult to achieve with fluorescent probes due to photo-bleaching and photo-toxicity..

To overcome these limitations, we employed Interferometric scattering (iSCAT) microscopy (12), a label free imaging technique that relies on the interference of the light scattered from nano-objects near a glass water interface with the light reflected by the same interface. The key advantage of light scattering over fluorescence detection is the lack of an upper limit to fluorescence emission rate and the absence of photobleaching, enabling high-speed ($> 1\text{kHz}$) recordings limited almost exclusively by the camera acquisition speed. For weak scatterers, the iSCAT signal-to-noise ratio has been shown to be roughly proportional to the square root of the incident light intensity, which theoretically limits the detection sensitivity to the incident laser power (12).

Here, we employ for the first time iSCAT microscopy to visualize membrane bound dynamic acto-myosin networks for tens of minutes with sub second frame rates. We characterize actin filament dynamics and myosin II filament binding times on sub-second time scales, while at the same time observing the large-scale network deformations and remodeling that occurs over minutes. Access to this wide range of time-scales will lead to a better understanding of the mechanics and dynamics on the molecular scale and how they translate into network dynamics on a mesoscopic scale. We demonstrate the potential of iSCAT microscopy to observe the intricate dynamics of two-dimensional active networks, providing a valuable addition to existing microscopy tools.

Results

We used iSCAT microscopy set-ups equipped with lasers of either 635nm or 445nm wavelength, to visualize thin films of acto-myosin networks bound via a deca His-SNAP-EzrinABD (actin binding domain) fusion protein (HSE) to supported lipid bilayers containing 98%_{mol} Dioleoyl-phosphocholine (DOPC) and 2%_{mol} 1,2-dioleoyl-sn-glycero-3-[(N-(5-amino-1-carboxypentyl)iminodiacetic acid)succinyl] (nickel salt) (Ni-NTA-DGS) as described earlier (11)(Fig. 1A). Due to the absence of any crowding factors or excess proteins, the actin and myosin II filaments were the principal sources of light scattering and could be clearly discerned using iSCAT microscopy (Fig. 1B). The contrast for actin filaments and myosin II filaments was about 20 times stronger when using the 445nm laser iSCAT setup compared to the 635nm laser set up (Sup Fig. 1A,B), because the 445nm laser setup was additionally equipped with a mask placed in the returning light path blocking major parts of the reflected light and thus increasing the signal-to-noise ratio (13).

Single filament dynamics in a static actin meshwork

Using the 445nm laser setup to record a membrane bound actin network, we visualized and studied the dynamics of short actin filaments within a network in the absence of myosin motors. To remove any signal originating from static structures such as immobile actin filaments or small impurities in the SLB, the image sequences were median filtered as described earlier (12) to reveal the mobile elements (Fig. 2A). Experiments in which we could observe the consecutive landing of actin filaments showed a step wise increase of the scattering interference signal (SupFig2 A,B; Video 1). This suggests that the iSCAT signal grows proportionally with the amount of protein in the region of interest and that the signal coming from actin can be translated into the number of actin filaments stacked on top of each other. Performing this analysis on images showing dense actin networks reveals that in the conditions used here ($[\text{actin}] = 100\text{--}350\text{nM}$), the actin layer comprises up to 6 filaments (Fig. 2B). The characteristic contrast profile of single actin filaments with constructive and destructive interference along the edge and center, respectively, is

used to identify and track the filament shape (see methods), its center of mass as well as its orientation (Fig. 2C, D; Video 2). The long acquisition time at high frame rates allows the detailed study of filament dynamics by computing the mean square displacement of the center of mass (MSD_{CM}) (Fig 2E). The MSD_{CM} ranging over three orders of magnitude in time indicate free diffusion of the short actin filament within the actin network (Fig 2E). Longer filaments ($> 2\mu m$) display a more restricted mobility with a more persistent orientation and a MSD trace that indicates confined diffusion (SupFig. 2 C,D).

iSCAT microscopy reveals binding dynamics of myosin II filaments to actin

We next characterize myosin II filament dynamics while interacting with the membrane bound actin filament network. First, we determined that our myosin II filaments have a characteristic length of $533(\pm 113)$ nm (445nm laser) and $556(\pm 115)$ nm (635 nm laser) (SupFig. 1C-F), respectively. This is in good agreement with previous measures of muscle myosin II filament length (10).

Second, we analyzed the binding/ unbinding dynamics of myosin II filaments to membrane bound actin filaments in the presence of ATP using the 635nm laser iSCAT setup. These dynamics are of special interest, because the dynamics of myosin filaments comprised of many myosin head domains cannot be easily described by models for the interaction between actin filaments and a single myosin motor protein. Myosin II filaments not only undergo rapid binding/ unbinding events of single myosin heads, but can also show multiple head binding events which leads to cooperative effects of motor binding and processive motor activity (14, 15). In addition, myosin filaments can exert forces on the actin filaments and either move persistently along an actin filaments or exhibit forces on actin filaments leading to the rupture of single actin filaments or contraction of multiple actin filaments (10, 11). Still, imaging with 5-10Hz for several minutes was sufficient to capture a broad range of myosin filament dynamics with high accuracy (Video 3). To remove any signal originating from static structures such as immobile actin filaments or small impurities in the SLB, the image sequences were median filtered (12). In a second step, a maximum projection of the time series was used to visualize the tracks occupied by myosin II filaments during the experiment. Lines following these tracks were then used to compute kymographs depicting the myosin II filament binding times and their motion along actin filaments (Fig 3A).

At an ATP concentration of about $100\mu M$, myosin II-actin binding times are widely spread with the majority following a single exponential decay with a time constant of $\tau = 2.2(\pm 0.4)$ sec, likely corresponding to single myosin head attachment/detachment. A second population of long lived binding times from 10-70sec was observed, probably corresponding to the un binding of multiple heads (Fig. 3B). At lower ATP concentrations, the system becomes contractile and exhibits large scale contractions (Video 4)(11, 16); correspondingly, the myosin II filament binding time increases to $\tau = 4.4(\pm 0.3)$ sec (Fig. 3C). Further analysis of the tracks in the kymographs reveal the differences in the dynamic properties of myosin II filament at high and low ATP levels. At high ATP levels, the mobile myosin II filaments travel with an average of $v_{myoII\text{ filament}} = 0.17(\pm 0.20)\mu m\text{ sec}^{-1}$, the run length (processivity) distribution decays exponentially with a decay factor of $\lambda = 0.30(\pm 0.03)\mu m$ (Fig. 3 D,E). Plotting run length versus binding time shows a weak positive correlation (Fig 3F) suggesting that it is indeed the engagement of an ensemble of myosin II heads of low duty ratio that leads to an effective high processivity of the myosin II filament as hypothesized earlier (17). At low ATP levels, when the network becomes contractile and the myosin II filament binding times longer, the mobile myosin II filaments travel with an average of $v_{myoII\text{ filament}} = 0.37(\pm 0.25)\mu m\text{ sec}^{-1}$, the run length decay factor is $\lambda = 1.09(\pm 0.06)\mu m$ and the correlation between run length and binding times is stronger with a majority of myosin II filaments showing

persistent movement at velocities $>0.4 \mu\text{msec}^{-1}$ for several seconds (Fig 3G-I). It is interesting to note that myosin II filaments move faster and for longer times at low ATP concentrations as a result of the slower unbinding dynamics of individual myosin heads at limited ATP levels. These features of single myosin II filament dynamics could serve as a molecular explanation for the large-scale contraction observed at low ATP levels.

Characterization of acto-myosin network dynamics

Turning to the full network dynamics, we focused on two states of the acto-myosin network, namely the contractile network at low ATP concentration and the remodeling state at high ATP concentration as described earlier (11). Since the long-term imaging does not affect the activity of myosin filaments or the integrity of actin filaments, we were able to observe the transition starting with a homogeneous network, followed by the formation of small clusters and ending by large cluster formation (Fig. 4A, Video 4). We quantified the changes in cluster length scales by computing the density-density autocorrelation function at each time-point, which indicates that clustering sets in after 700sec of remodeling and then proceeds continuously into larger scales (Fig. 4B).

The frame rate of 10 Hz enabled us to use particle image velocimetry (PIV) to analyze the myosin II generated flows of the acto-myosin network in the remodeling and contractile states, respectively. The resulting vector fields accounting for the flow velocities can be used to compute the local divergence and reveal the contractile regions (negative divergence) of the acto-myosin network in the contractile state (Fig. 4C). To compare the network dynamics in the contractile versus the remodeling state, we computed the network velocity distribution in both conditions (Fig. 4E). As expected, the network velocities are higher in the contractile state with the mean velocity $v_{\text{network}} = 74 (\pm 64) \text{ nm}$ whereas $v_{\text{network}} = 14 (\pm 14) \text{ nm}$ in the remodeling state. This observation correlates with the difference in the binding times of myosin II filaments to actin filaments with short interaction times in the remodeling state (Fig. 3 B) compared to the longer times in the contractile state (Fig. 3C) and the corresponding changes in run length at low ATP concentrations (Fig. 3E, H).

Sustained vortex formation by the acto-myosin network

Remarkably, we could observe the formation of spirals and vortices of the acto-myosin network at low ATP concentrations in some of our experiments (Fig. 4F, Video 5). These vortices were characterized by multiple myosin II filaments moving around a common central point, they extended radially for 1-5 μm and sustained for several minutes. PIV on single vortices showed a general circular flow around the center with a velocity profile that peaks at about half of the vortex radius (Fig. 4G, H), which is in good agreement with earlier theoretical work (18, 19). Although vortex formation is expected for active gels of polar filaments, it was experimentally realized and described in microtubule networks, but, to our knowledge, not yet in acto-myosin networks. This is most likely due to the experimental conditions used here, i.e. the actin filament length (5-10 μm), the actin to myosin ratio (4:1 monomer ratio), the supported lipid bilayer providing the acto-myosin network with a two-dimensional fluid scaffold and the sustained high myosin activity in the absence of photo-damage.

Taken together, we demonstrate that the unique features of iSCAT microscopy allow one to capture and study single particle as well as ensemble dynamics on the multiple micrometer scale ranging from milliseconds up to tens of minutes, making it a versatile tool for the understanding of complex, biomimetic motor-filament networks.

Discussion

Here we demonstrate how iSCAT microscopy can be used to observe complex, multi component systems such as the lipid membrane anchored acto-myosin network deployed as a thin film. Employing different laser wavelengths allows one to focus on elements of a certain size, e.g. the signal from single actin filaments is prominent using the 445nm laser whereas they provide poor contrast at 635nm wavelength. At the same time, myosin filaments may be visualized with both the 445nm and the 635nm laser, providing a simple way to distinguish the two filaments types based on the contrast values. iSCAT microscopy offers great advantages for many reconstituted systems by not requiring any protein labeling or fixation and by visualizing all elements present in the system at image acquisition rates up to the kHz range only limited by the intensity of the incident laser beam and the camera acquisition rate (12).

High frequency imaging is used to perform single particle tracking inside static actin networks and filament shape analysis of the actin filaments would be possible as well. The absence of photo damage and long imaging sequences facilitate the analysis of particle diffusion over several orders of magnitude in the time domain (0.1-1000 sec), providing more detailed insights into the diffusion of filaments within complex networks which is otherwise difficult to achieve with other microscopy techniques.

The study of myosin II filament binding dynamics to actin inside the membrane bound, remodeling acto-myosin network provides new insights into the physico-chemical mechanism of acto-myosin contractility in an ensemble. This augments our understanding from bulk measurements, and allows an analysis of these ensembles in terms of their microscopic elements, as local, single particle measurements. Based on the myosin II filament run lengths depicted in (Fig. 3E) and (Fig. 3H) we estimated the effective duty-cycle ratio of the myosin II filaments using a step size of 8nm as reported for muscular myosin II (20). Applying the relation between the step-number distribution $n_{obs}(x)$ of a myosin motor and the effective duty-cycle ratio r of a myosin filament (21)

$$[1] \quad \frac{N_{obs}(x)}{N_{obs}(1)} = n_{obs}(x) = (2r - r^2)^{(x-1)}$$

we estimated that at high ATP levels ($>100 \mu\text{M}$) the effective duty-cycle ratio is $r_{high ATP} = 0.841 (\pm 0.004)$ and $r_{low ATP} = 0.906 (\pm 0.002)$ at low ATP levels ($<10 \mu\text{M}$). If we assume now in a very simple model that n head domains of a myosin II filament can interact independent with an actin filament described by the single head domain duty-cycle ratio r_{hd} (21, 22), then we can obtain r_{hd} from the effective filament duty-cycle ratio r using the relation

$$[2] \quad r_{hd} = 1 - (1 - r)^{1/n}$$

With $n = 120$ head domains, which is a typical number for muscular myosin II filaments (22), we obtain single myosin II head domain duty cycle ratios of about 0.01 - 0.03 for high, and low ATP levels, respectively, which is in good agreement with reported values of single muscular myosin II head domains of $r_{hd} = 0.04$ (23). We would like to emphasize that these numbers are only rough estimates based on a very simplified model of myosin filaments, but it demonstrates a strategy how minute changes in the single myosin head domain properties can be linked to big differences in the properties of myosin filaments with consequences for the acto-myosin network. Longer binding times and persistent motion of myosin filaments promote the transmission of stresses over longer distances leading to a switch from a remodeling to a contractile state. In addition to binding times described by a single exponential decay

consistent with an effective myosin filament duty-cycle ratio, our iSCAT studies reveal a second population of myosin II filaments with very long binding times. It remains to be elucidated whether the long binding time population is due to dead heads or to another cooperative effect of multiple myosin heads binding to actin filaments. Longer Future studies using non-muscular myosin II constructs which allow tight control of the number of functional head domains will be ideal for this (24).

Myosin II filament dynamics were either extrapolated based on studies of single myosin head domains and single motor proteins (25), or on studies on whole myosin fibers (26). Whereas these approaches do not permit the study of cooperative effects of multiple myosin head domains within a myosin II filament on the actin binding kinetics, the present work demonstrates how iSCAT microscopy brings such studies within reach of a quantitative analysis.

The capacity to follow all network components over long time with high temporal resolution allows one to put observed, individual myosin II filament binding dynamics in relation to the local activity and stresses transmitted to the actin network, e.g. by the application of PIV. We show that PIV reveals regions of negative divergence in the acto-myosin flow fields characteristic of contractile networks (18, 27). Interestingly, these contractile regions are stable over time scales of 100sec and seem to constitute a steady state where myosin II filaments continue to travel towards existing myosin clusters and detach before getting jammed in the cluster. The observation of vortices represents another active steady state that was predicted in a theoretical work on active gels by Kruse and colleagues (18). It is exciting that these structures, which were observed recently in live cells (28), could now be realized for the first time in a reconstituted system. It is likely that earlier studies did simply not employ the right concentration of actin and myosin to foster vortex formation or that the ability to observe the system for longer times without any photodamage favored vortices, but more detailed studies will be needed to understand better, why such structures were not reported in earlier studies. Exploring the network dynamics and its contractile behavior as a function of actin, myosin and ATP concentration, and to compare this with theoretical predictions will be of interest to gain deep insights into such active systems and iSCAT microscopy will be a valuable tool in this endeavor.

Materials and Methods

Purified Proteins

Actin was purified from chicken breast following the protocol from Spudich and Watt (29) and kept on ice in monomeric form in G-buffer (2 mM Tris Base, 0.2 mM ATP, 0.5 mM TCEP-HCl, 0.04% NaN₃, 0.1 mM CaCl₂, pH 7.0); Myosin II was obtained from chicken breast following a modified protocol from Pollard (30) and kept in monomeric form in myo-buffer (500 mM KCl, 1 mM EDTA, 1 mM DTT, 10 mM HEPES, pH 7.0). The day prior to experiments, functional myosin II proteins are separated from proteins containing dead head domains by a round of binding and unbinding to F-actin at a 5:1 actin to myosin ratio (switch from no ATP to 3 mM ATP) followed by a spin at 60000 rpm for 10 min at 4°C in a TLA100.3 rotor. The supernatant containing functional myosin II is dialyzed against myo-buffer over-night and used for experiments for up to three days.

To link actin to the SLB, we used a construct containing 10x His domains followed by a linker (KCK) and the actin binding domain of Ezrin as described earlier (11)

Supported Lipid Bilayer and Experimental Chamber Preparation

Glass coverslips (#1.5 borosilicate, Menzel, Germany) for SLB formation were cleaned with Hellmanex III (Hellma Analytics, Mühleim, Germany) following the manufacturer's instructions followed by thorough rinses with EtOH and MilliQ water, blow dried with N₂ and finally passed briefly over a Bunsen burner flame. For the experimental chamber, 0.2 ml PCR tubes (Tarsons Products, Kolkata, India) were cut to remove the lid and the conical bottom part and stuck to the cleaned glass using UV glue (NOA88, Norland Products, Cranbury, NJ) and three minutes curing by intense UV light at 365nm (PSD-UV8T, Novascan, Ames, IA). Freshly cleaned and assembled chambers were directly used for experiments.

Supported lipid bilayers (SLB) were formed by fusion of small uni-lamellar vesicles (SUV). Lipid mixtures containing 98% DOPC and 2% DGS-NTA(Ni²⁺) were mixed together with 1ml chloroform (Electron Microscopy Sciences, Hatfield, PA) in a cleaned amber glass vial (B7990-2A, Thermo Fisher Scientific, Rockwood, TN), dried under a N₂ stream, placed in a vacuum desiccator overnight and resuspended in SUV storage buffer (150 mM NaCl, 20 mM HEPES, 5% sucrose, pH 7.2) to a final lipid concentration of 4 mM. SUVs of ~80 nm diameter were formed by the extrusion method using a lipid extruder (Avanti Polar Lipids Inc.) with an 80 nm pore size polycarbonate filter membrane (GE Whatman, Piscataway, NJ).

For SLB formation, 10-20 µl of SUV mix were added to 100 µl of SLB formation buffer (150 mM NaCl, 2 mM CaCl₂, 20 mM Hepes, pH 5.5), incubated for 20 min at RT and washed ten times with SLB working buffer (150 mM NaCl, 20 mM HEPES, 0.1 mg/ml β-casein, pH 7.2). For experiments with F-actin, SLB working buffer was replaced by 100 µl KMEH (50 mM KCl, 2 mM MgCl₂, 1 mM EGTA, 20 mM HepesHEPES, pH 7.2).

Formation of Acto-Myosin Network

In a typical experiment, 10 nM HKE were added to SLBs and incubated for 40min followed by three washes with KMEH. During this incubation time, F-actin was polymerized by addition of 10%_{vol} of 10x ME buffer (100 mM MgCl₂, 20 mM EGTA, pH 7.2) to the G-actin stock and 2min incubation to replace G-actin bound Ca²⁺ ions with Mg²⁺. Polymerization buffer was added to induce F-actin polymerization in a test tube at a final G-actin concentration of 5 µM in KMEH supplemented with 2 mM ATP. After 20-30 min incubation, the desired amount of F-actin was added to the SLBs using blunt cut 200 µl pipette tips. An incubation of 30 min allowed the F-actin layer to bind to the SLB at steady state, myosin II filaments were added afterwards and the evolution of the acto-myosin system was observed for up to 90 min. To induce remodelling of the acto-myosin system, Mg-ATP (100 mM) was added to a final concentration of 1 mM. Each step of this procedure was performed on the microscope stage, which allowed us to check its state continuously. The open chamber design allowed the addition of each component from top without induction of flows that would perturb the actin network.

iSCAT microscopes

Interferometric scattering microscopy was performed on two different home-built setups similar to those detailed in (13, 31). Briefly, a weakly focused laser beam was scanned across the sample over an area of $24 \times 24 \mu\text{m}^2$ (445 nm laser) or $32.6 \times 32.6 \mu\text{m}^2$ (635 nm laser). The light reflected from the water-glass interface together with the scattered light from the sample was imaged onto a CMOS camera (445 nm laser: Point Grey GS3-U3-23S6M-C, Flir, Canada; 635 nm laser: MV-D1024-160-CL-8, Photonfocus, Switzerland). The cameras were controlled using home-written Labview software. The setup with the 445 nm laser had a 3.5 mm partially reflective mirror placed in the re-imaged back focal plane of the objective for enhanced scattering contrast as described in Cole et al. ACS Photonics 2017. The videos were recorded at 10 fps (445 nm laser) and 5 fps (635 nm laser) with the illumination intensity on the sample (445 nm laser: 250 W/cm²; 635 nm laser: 1.9 kW/cm²) set to nearly saturate the camera with the returning light. The pixel sizes were 23.4 nm/pixel (445 nm laser) and 31.8 nm/pixel (635 nm laser).

Image processing

Non-sample specific illumination inhomogeneities, fixed-pattern noise and constant background were removed from the raw images by dividing each of them with a flat field image that contained only these features. The flat field image was computed by recording 2000 frames of the sample while moving the stage. For each pixel, a temporal median was calculated resulting in a flat field image that only contained static features.

Median filtering

Movies were median filtered using Matlab (MathWorks, Natick, MA, USA). For each image sequence, the median is computed for each pixel, deleted from the original image sequence and the median filtered image sequence as well as the computed median filter are saved.

Actin filament tracking

Actin filaments that became visible after median filtering and that did not cross other actin filaments for at least 1000 frames were tracked using image J (<http://imagej.nih.gov>) and the plugin JFilament (<http://athena.physics.lehigh.edu/jfilament>). The obtained tracking traces were analyzed using Matlab to compute the position of the center of mass (CM) for each time point and to generate plots of the CMs mean square displacement.

Myosin binding dynamics

Median filtered image sequences were inverted, from which maximum projections were generated to reveal regions of myosin II filament binding (i.e. actin filaments). Lines were drawn along those regions and used to generate kymographs (kymograph tool in Image J, line width 3), which were analyzed afterwards manually to measure binding times and run lengths. The resulting velocity distribution, run length distribution and correlation between run length and bound time were plotted using OriginPro 2016 (OriginLab Corporation, Northampton, MA, USA).

Particle Image Velocimetry

Particle Image Velocimetry (PIV) was performed using PIVlab (32, 33) (Garcia, D. (2011): A fast all-in-one method for automated post-processing of PIV data. Experiments in Fluids, Springer-Verlag, 2011, 50, 1247-1259). Median filtered image sequences were inverted and transformed into 8-bit format using Image J. The PIV vector maps were computed with the FFT window deformation algorithm and the window sizes of 64, 32 and 16 pixels and step sizes of 32, 16 and 8 pixels, respectively. The accepted range of velocity vectors was limited to $\pm 2 \mu\text{m sec}^{-1}$. *Intensity autocorrelation*

Image sequences were inverted before the intensity autocorrelation, $\chi(\vec{x}) = \langle \delta_I(\vec{y}) \delta_I(\vec{y} + \vec{x}) \rangle$
 $\chi(\vec{x}) = \langle \delta_I(\vec{y}) \delta_I(\vec{y} + \vec{x}) \rangle$, was computed in Matlab with a fast Fourier transform and summed over the angular coordinate to obtain $\chi(r)$.

Contributions:

DK conceived, designed and performed experiments, analyzed data, wrote manuscript; NH helped in the experiments, analyzed data, wrote manuscript; GY and AF did set up the iSCAT microscopes; PK conceived experiments, wrote manuscript; SM wrote manuscript.

Acknowledgements

DK thanks Madan Rao and Kabir Husain (NCBS) for instructive discussions and comments on the manuscript and the Company of Biologists for supporting this work with a Travelling fellowship. DK was supported by a postdoctoral fellowship of NCBS; NH was supported by a postdoctoral research fellowship of the Deutsche Forschungsgemeinschaft (DFG); GY was supported by a Zvi and Ofra Meitar Magdalen Graduate Scholarship; PK was supported by an ERC Starting Investigator Grant (Nanoscope, 337577); SM was a JC Bose fellowship DST and HFSP.

References:

1. Kusumi, A., C. Nakada, K. Ritchie, K. Murase, K. Suzuki, H. Murakoshi, R.S. Kasai, J. Kondo, T. Fujiwara, and Hideji Murakoshi. 2005. Paradigm shift of the plasma membrane concept from the two-dimensional continuum fluid to the partitioned fluid: high-speed single-molecule tracking of membrane molecules. Annu. Rev. Biophys. Biomol. Struct. 34: 351–78.
2. Arumugam, S., and P. Bassereau. 2015. Membrane nanodomains: contribution of curvature and interaction with proteins and cytoskeleton. Essays Biochem. 57: 109–19.
3. Saka, S.K., A. Honigsmann, C. Eggeling, S.W. Hell, T. Lang, and S.O. Rizzoli. 2014. Multi-protein assemblies underlie the mesoscale organization of the plasma membrane. Nat. Commun. 5: 1–14.
4. Rao, M., and S. Mayor. 2014. Active organization of membrane constituents in living cells. Curr. Opin. Cell Biol. 29C: 126–132.

5. van Zanten, T.S., A. Cambi, M. Koopman, B. Joosten, C.G. Figdor, M.F. Garcia-Parajo, and T.S. Van Zanten. 2009. Hotspots of GPI-anchored proteins and integrin nanoclusters function as nucleation sites for cell adhesion. *Proc. Natl. Acad. Sci. U. S. A.* 106: 18557–62.
6. Plowman, S.J., C. Muncke, R.G. Parton, and J.F. Hancock. 2005. H-ras, K-ras, and inner plasma membrane raft proteins operate in nanoclusters with differential dependence on the actin cytoskeleton. *Proc. Natl. Acad. Sci. U. S. A.* 102: 15500–5.
7. Köster, D. V, and S. Mayor. 2016. Cortical actin and the plasma membrane: inextricably intertwined. *Curr. Opin. Cell Biol.* 38: 81–89.
8. Murrell, M.P., and M.L. Gardel. 2012. F-actin buckling coordinates contractility and severing in a biomimetic actomyosin cortex. *Proc. Natl. Acad. Sci. U. S. A.* .
9. Vogel, S.K., F. Heinemann, G. Chwastek, and P. Schwille. 2013. The design of MACs (Minimal Actin Cortices). *Cytoskeleton.* : n/a-n/a.
10. Ideses, Y., A. Sonn-Segev, Y. Roichman, and A. Bernheim-Groswasser. 2013. Myosin II does it all: assembly, remodeling, and disassembly of actin networks are governed by myosin II activity. *Soft Matter.* 9: 7127.
11. Köster, D.V., K. Husain, E. Iljazi, A. Bhat, P. Bieling, R.D. Mullins, M. Rao, and S. Mayor. 2016. Actomyosin dynamics drive local membrane component organization in an in vitro active composite layer. *Proc. Natl. Acad. Sci.* 113: E1645–E1654.
12. Ortega Arroyo, J., D. Cole, and P. Kukura. 2016. Interferometric scattering microscopy and its combination with single-molecule fluorescence imaging. *Nat. Protoc.* 11: 617–633.
13. Cole, D., G. Young, A. Weigel, A. Sebesta, and P. Kukura. 2017. Label-Free Single-Molecule Imaging with Numerical-Aperture-Shaped Interferometric Scattering Microscopy. *ACS Photonics.* 4: 211–216.
14. Bidone, T.C., W. Jung, D. Maruri, C. Borau, R.D. Kamm, T. Kim, M. Gardel, K. Kasza, C. Brangwynne, J. Liu, D. Weitz, M. Murrell, P. Oakes, M. Lenz, M. Gardel, E. Reichl, Y. Ren, M. Morphew, M. Delannoy, J. Effler, K. Girard, T. Bidone, H. Tang, D. Vavylonis, D. Laporte, N. Ojkic, D. Vavylonis, J. Wu, S. Tojkander, G. Gateva, P. Lappalainen, D. Burnette, S. Manley, P. Sengupta, R. Sougrat, M. Davidson, B. Kachar, P. Hotulainen, P. Lappalainen, D. Gordon, A. Bernheim-Groswasser, C. Keasar, O. Farago, Y. Inoue, S. Tsuda, K. Nakagawa, M. Hojo, T. Adachi, K. Popov, J. Komianos, G. Papoian, M. Lenz, M. Mak, M. Zaman, R. Kamm, T. Kim, P. Underhill, P. Doyle, G. Bell, T. Kim, H. Ennomani, G. Letort, C. Guérin, J.-L. Martiel, W. Cao, F. Nédélec, A.-C. Reymann, R. Boujemaa-Paterski, J.-L. Martiel, C. Guérin, W. Cao, H. Chin, W. Jung, M. Murrell, T. Kim, T. Erdmann, U. Schwarz, T. Erdmann, P. Albert, U. Schwarz, L. Cramer, M. Siebert, T. Mitchison, P. Oakes, Y. Beckham, J. Stricker, M. Gardel, C. Borau, T. Kim, T. Bidone, J. García-Aznar, R. Kamm, T. Kim, W. Hwang, R. Kamm, T. Kim, W. Hwang, H. Lee, et al. 2017. Morphological Transformation and Force Generation of Active Cytoskeletal Networks. *PLOS Comput. Biol.* 13: e1005277.
15. Albert, P.J., T. Erdmann, and U.S. Schwarz. 2014. Stochastic dynamics and mechanosensitivity of myosin II minifilaments. *New J. Phys.* 16.
16. Smith, D., F. Ziebert, D. Humphrey, C. Duggan, M. Steinbeck, W. Zimmermann, and J. Käs. 2007. Molecular motor-induced instabilities and cross linkers determine biopolymer organization. *Biophys. J.* 93: 4445–52.
17. Erdmann, T., and U.S. Schwarz. 2012. Stochastic force generation by small ensembles of myosin II

- motors. *Phys. Rev. Lett.* 108: 1–5.
18. Kruse, K., J.F. Joanny, F. Julicher, J. Prost, and K. Sekimoto. 2004. Asters , Vortices , and Rotating Spirals in Active Gels of Polar Filaments. *Phys. Rev. Lett.* 92: 1–4.
19. Husain, K., and M. Rao. 2017. Emergent Structures in an Active Polar Fluid: Dynamics of Shape, Scattering, and Merger. *Phys. Rev. Lett.* 118: 1–5.
20. Toyoshima, Y.Y., S.J. Kron, and J.A. Spudich. 1990. The myosin step size : Measurement of the unit displacement per ATP hydrolyzed in an in vitro assay. *Proc. Natl. Acad. Sci.* 87: 7130–7134.
21. Veigel, C., F. Wang, M.L. Bartoo, J.R. Sellers, and J.E. Molloy. 2002. The gated gait of the processive molecular motor, myosin V. *Nat. Cell Biol.* 4: 59–65.
22. Nagy, A., Y. Takagi, N. Billington, S.A. Sun, D.K.T. Hong, E. Homsher, A. Wang, and J.R. Sellers. 2013. Kinetic characterization of nonmuscle myosin IIB at the single molecule level. *J. Biol. Chem.* 288: 709–722.
23. Harris, D.E., and D.M. Warshaw. 1993. Smooth and skeletal muscle myosin both exhibit low duty cycles at zero load in vitro. *J. Biol. Chem.* 268: 14764–14768.
24. Billington, N., A. Wang, J. Mao, R.S. Adelstein, and J.R. Sellers. 2013. Characterization of three full-length human nonmuscle myosin II paralogs. *J. Biol. Chem.* 288: 33398–33410.
25. Kovacs, M., K. Thirumurugan, P.J. Knight, and J.R. Sellers. 2007. Load-dependent mechanism of nonmuscle myosin 2. *Proc. Natl. Acad. Sci.* 104: 9994–9999.
26. Burton, K. 1992. Myosin step size: Estimates from motility assays and shortening muscle. *J. Muscle Res. Cell Motil.* 13: 590–607.
27. Gowrishankar, K., and M. Rao. 2015. Nonequilibrium phase transitions, fluctuations and correlations in an active contractile polar fluid. *Soft Matter.* 1201.3938.
28. Fritzsche, M., D. Li, H. Colin-York, V.T. Chang, E. Moeendarbary, J.H. Felce, E. Sezgin, G. Charras, E. Betzig, and C. Eggeling. 2017. Self-organizing actin patterns shape membrane architecture but not cell mechanics. *Nat. Commun.* 8: 14347.
29. Spudich, J.A., and S. Watt. 1971. The regulation of rabbit skeletal muscle contraction. I. Biochemical studies of the interaction of the tropomyosin-troponin complex with actin and the proteolytic fragments of myosin. *J. Biol. Chem.* 246: 4866–71.
30. Pollard, T.D. 1982. Myosin purification and characterization. *Methods Cell Biol.* 24: 333–71.
31. Ortega-Arroyo, J., and P. Kukura. 2012. Interferometric scattering microscopy (iSCAT): new frontiers in ultrafast and ultrasensitive optical microscopy. *Phys. Chem. Chem. Phys.* 14: 15625.
32. Thielicke, W., and E.J. Stamhuis. 2014. PIVlab – Towards User-friendly, Affordable and Accurate Digital Particle Image Velocimetry in MATLAB. *J. Open Res. Softw.* 2.
33. Thielicke, W. 2014. The Flapping Flight of Birds - Analysis and Application. .

Figure 1, experimental setup: **A)** Diagram of the in-vitro system consisting of a supported lipid bilayer (SLB), actin-membrane linker protein His10-KCK-EzrinABD, actin filaments and myosin II filaments. **B)** Example images of actin filaments (left) and myosin II filaments (right) recorded with the 445 nm laser iSCAT system; scale bar: 2 μm . **C)** Histogram depicting the interferometric contrast distribution along actin filaments (grey, $N_{\text{fil}}=12$, $N_{\text{measure}}=562$) and myosin II filaments (magenta, $N_{\text{fil}}=5$, $N_{\text{measure}}=96$).

Figure 2, single actin filament dynamics in an actin network: **A)** Dynamic features are visualised by subtracting the image sequence median from the raw images (left: raw image, right: median filtered); grey bar depicts the contrast range, scale bar: 5 μm . **B)** Histogram of the actin layer thickness in a typical experiment based on local interferometric contrast measurements divided by the contrast value of an individual actin filament ($N=149$). **C)** Image sequence depicting the dynamics of a single actin filament (red dashed line) inside an acto-myosin network; scale bar: 1 μm . **D)** Corresponding trajectory of the filament in (C) over time, small dots depict the tracked filament, bold dots its center of mass, color indicates the time. **E)** mean square displacement of the filament's center of mass shown in (D).

Figure 3, myosin II filament dynamics in the acto-myosin network at different ATP concentrations: **A)** Kymograph depicting myosin dynamics along static actin filaments generated from median filtered image sequences on the 635nm laser iSCAT setup. White lines correspond to myosin II filaments that are moving along actin filament. **B)** Histogram of myosin II binding times to actin filaments at high ATP levels ($>100 \mu\text{M}$) ($N=6400$). **C)** Histogram of myosin II binding times to actin filaments at low ATP levels ($< 10 \mu\text{M}$) ($N=8000$). **D-F)** Histograms of the myosin II filament velocities (D), run lengths (E) and frequency plot of run length vs binding time (F) extracted from myosin II filament kymographs at high ATP levels ($>100 \mu\text{M}$) ($N=1283$). **G-I)** Histograms of the myosin II filament velocities (G), run lengths (H) and frequency plot of run length vs binding time (I) extracted from myosin II filament kymographs at low ATP levels ($< 10 \mu\text{M}$) ($N=1840$). Red lines depict fitted functions to describe the parameter distributions (single exponential function in (B,C, E and H), normal distribution in (D and G).

Figure 4, dynamics of contracting acto-myosin networks: **A)** Image sequence depicting the dynamics of a membrane bound acto-myosin network acquired with the 445nm laser iSCAT setup; experimental conditions: [actin] = 250 nM, [capping protein] = 0.5 nM, [myosin II] = 30 nM, [ATP] = 50 μM ; scale bar: 3 μm . **B)** Corresponding density-density correlation illustrating the network contraction in the rise of correlation length at later time points. **C)** Image depicting the acto-myosin flow field (green vectors) computed by particle image velocimetry; scale bar 2 μm . **D)** The corresponding divergence map indicating regions of contractility (negative divergence, purple) at sites of acto-myosin clusters. **E)** Histogram of the acto-myosin flow distribution computed by PIV of acto-myosin networks at high ($>100 \mu\text{M}$, red) and low ($<10 \mu\text{M}$, black) ATP levels. **F)** Averaged signal over 120sec displaying an acto-myosin vortex (Video 5; scale bar 1 μm . **G)** Corresponding velocity profile averaged over 120 sec computed with PIV. Experimental conditions in (C-G): [actin] = 300nM, [myosin II] = 80 nM.

Sup Figure 1, comparison of the 445nm and 635nm laser iSCAT set ups: **A)** Histogram of actin filament contrast measurements with the 445nm laser iSCAT setup, and fit of the first peak corresponding to the single actin filament signal. **B)** Histogram of actin filament contrast measurements with the 635nm laser iSCAT setup, and fit of the first peak corresponding to the single actin filament signal. **C)** example image of an acto-myosin network with the 445 nm iSCAT setup highlighting present myosin filaments (red arrows). **D)** Histogram of myosin II filament length measurements with the 445nm laser iSCAT setup, showing a normal distribution (red line)(N=89). **E)** example image of an acto-myosin network with the 635 nm iSCAT setup highlighting present myosin filaments (red arrows). **F)** Histogram of myosin II filament length measurements with the 635nm laser iSCAT setup, showing a normal distribution (red line)(N=118).

Sup Figure 2, single actin filament dynamics: **A)** Images sequence of actin filaments landing on an SLB imaged with the 445nm iSCAT setup. **B)** Corresponding measurement of the interferometric contrast of the region depicted by the white square in (A) showing a stepwise increase of the signal with an actin filament landing on top of another. **C)** Trajectory of a long actin filament confined by the surrounding actin network, small dots depict the tracked filament, bold dots its center of mass, color indicates the time. **D)** Mean square displacement of the filament's center of mass shown in (C) (blue), the diversion from the red line (depicting the expected MSD of a free diffusing particle) at higher time scales indicates the confinement of the filament.

Sup Figure 3, estimation of effective myosin II filament duty ratios: **A)** plot of data from (Fig. 3E) converted into number of myosin head domain steps and fit of the equation [1] to estimate the effective duty ratio of myosin II filaments. **B)** plot of data from (Fig. 3H) converted into number of myosin head domain steps and fit of the equation from [1] to estimate the effective duty ratio of myosin II filaments.

Video 1 Movie showing the increase in interferometric scattering when one actin filament lands on top of another depicted in SupFig 2A,B

Video 2 Movie showing the actin filament depicted in Fig 2C

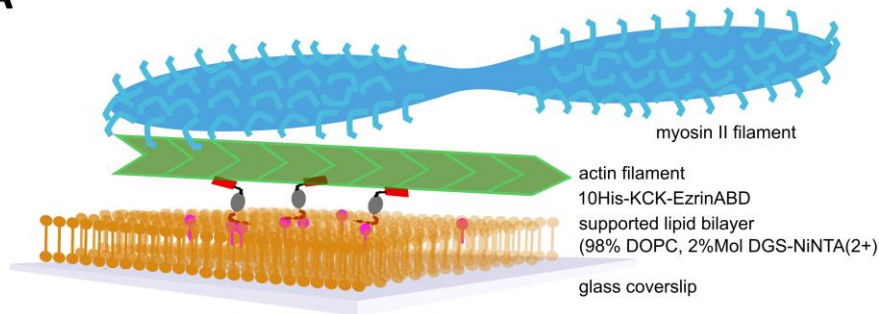
Video 3 Movie showing myosin II filament motion along actin filaments (arrow heads) as analyzed in Fig3

Video 4 Movie showing the transition of the acto-myosin network from a homogeneous to a clustered state as analyzed in Fig 4A,B.

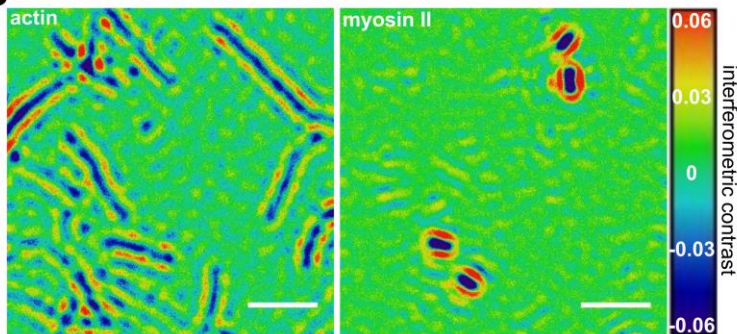
Video 5 Movie showing the myosin II filament dynamics forming a vortex analyzed in Fig 4F-H; interferometric scattering signal was inverted and images were converted into 8-bit format for analysis in PIVlab.

Figure 1

A



B



C

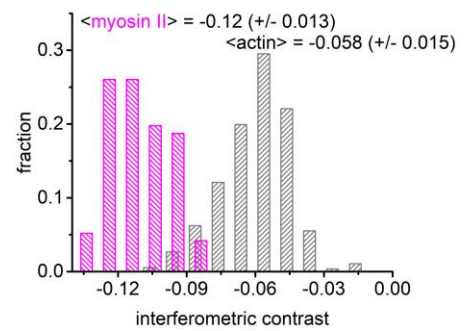


Figure 2

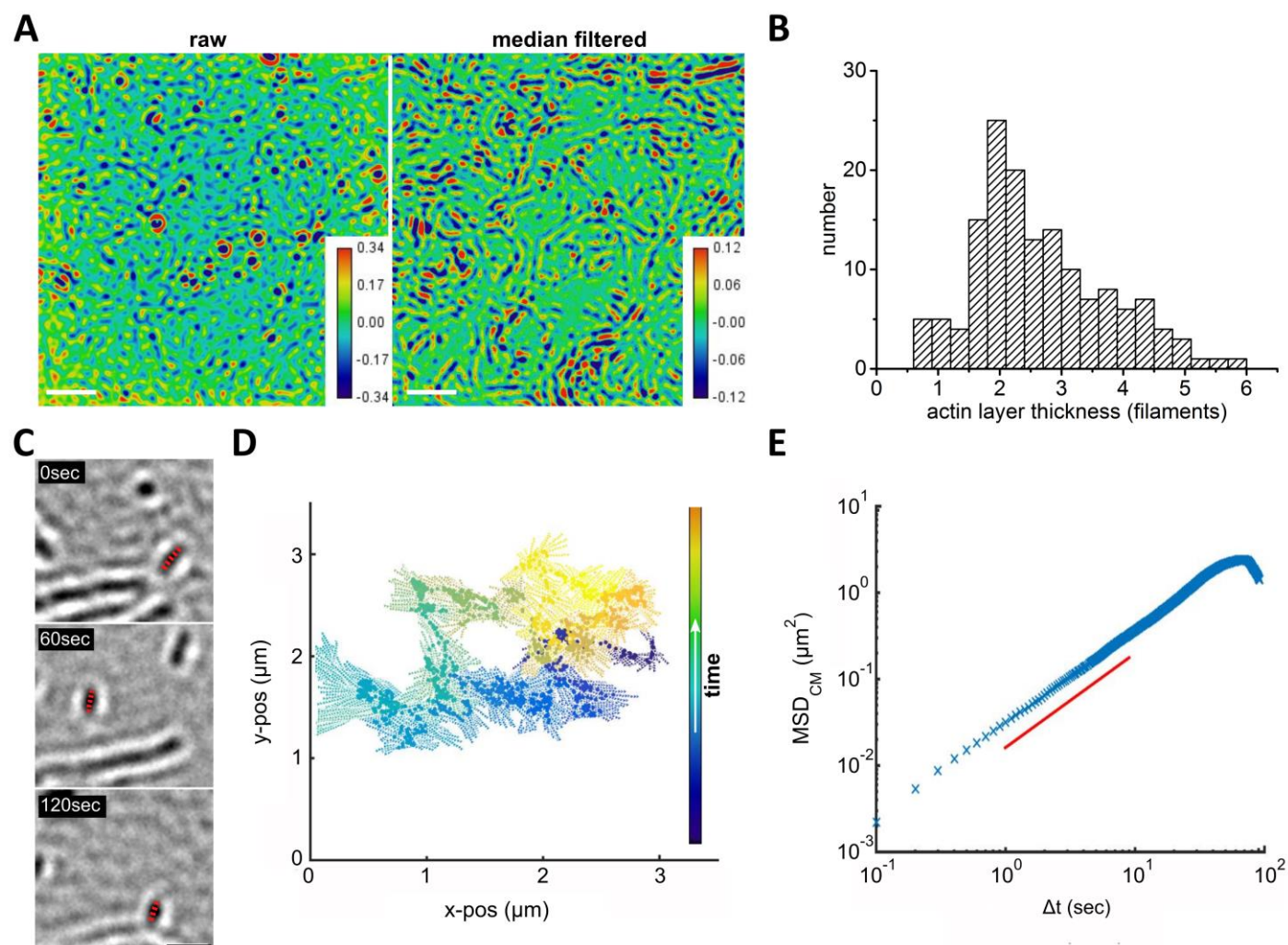


Figure 3

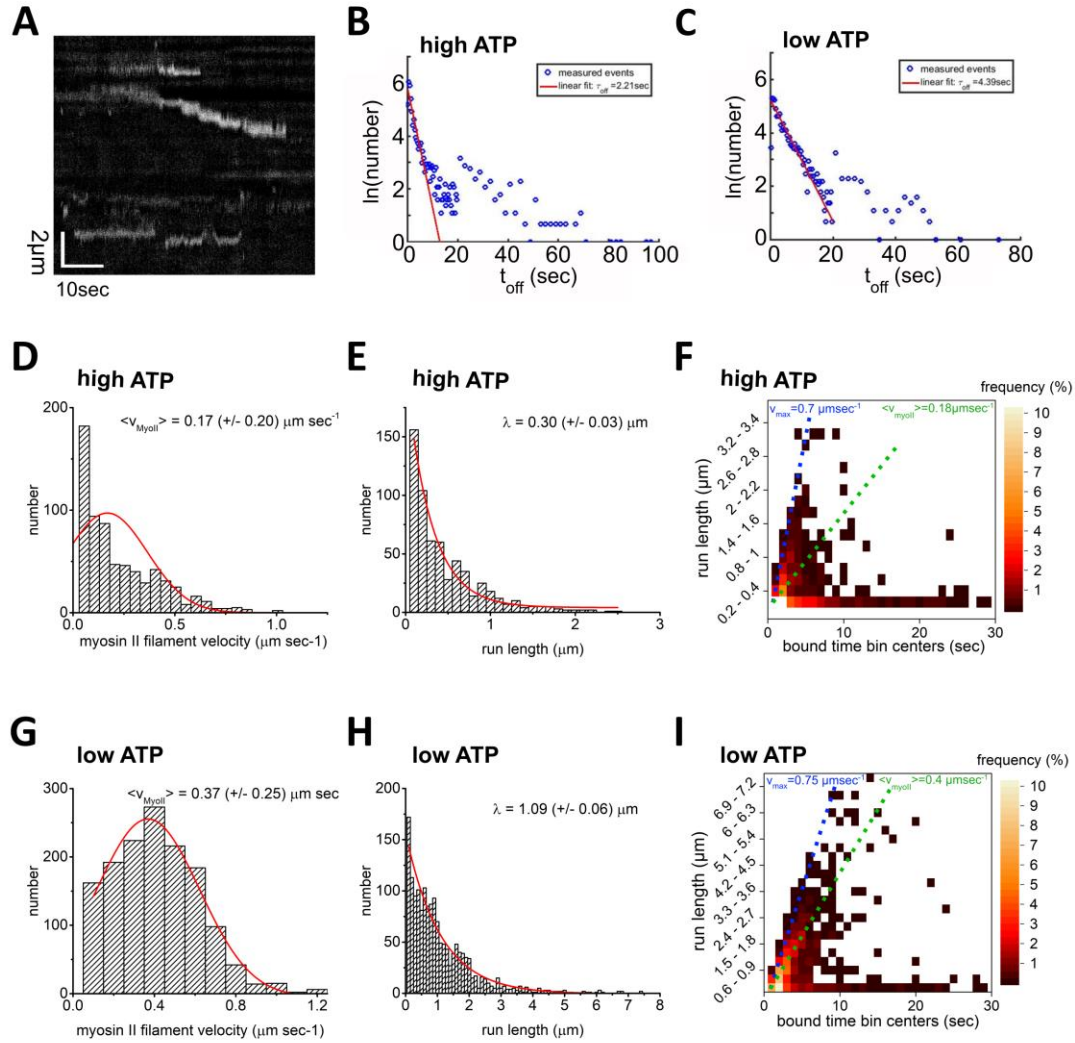
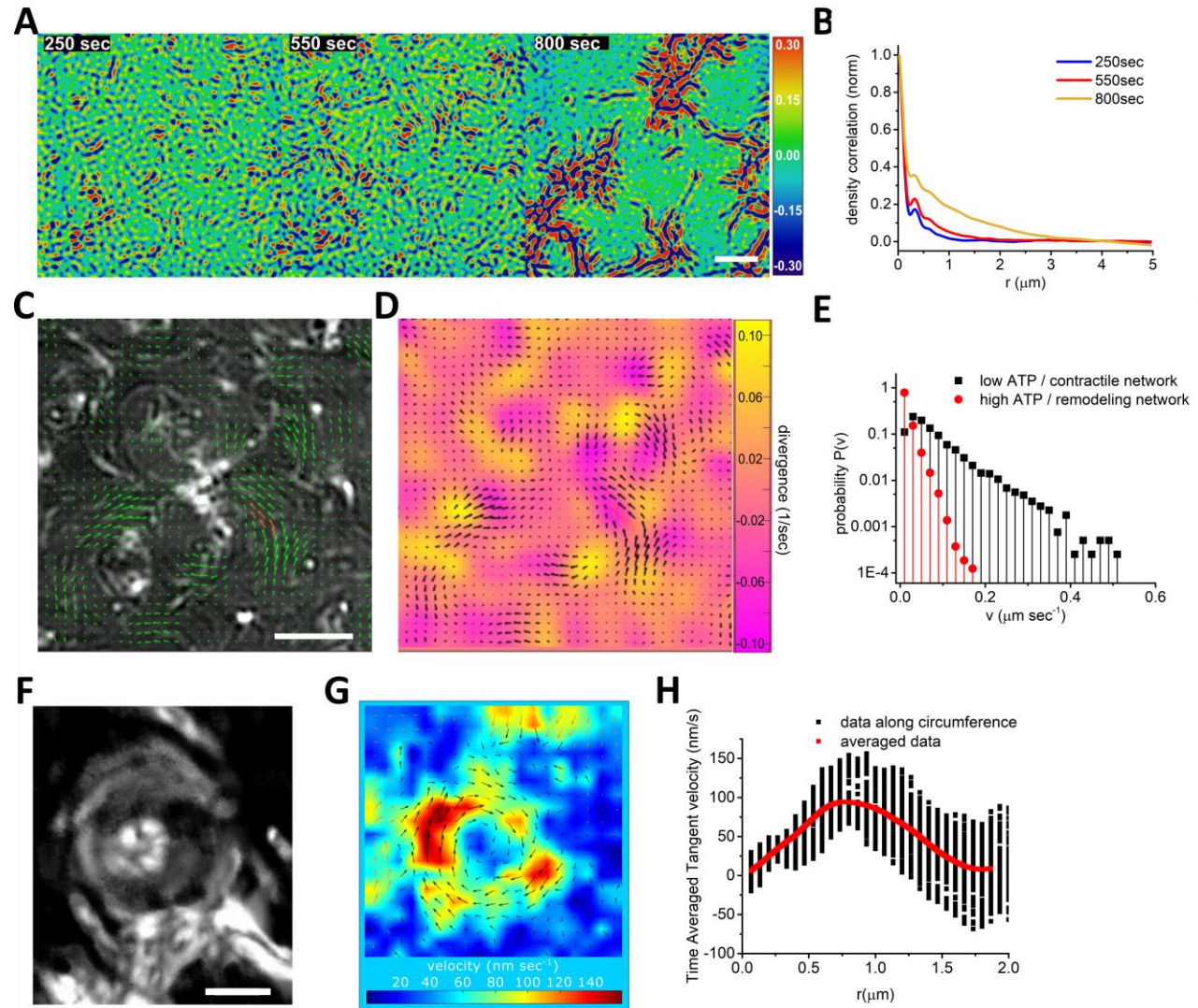
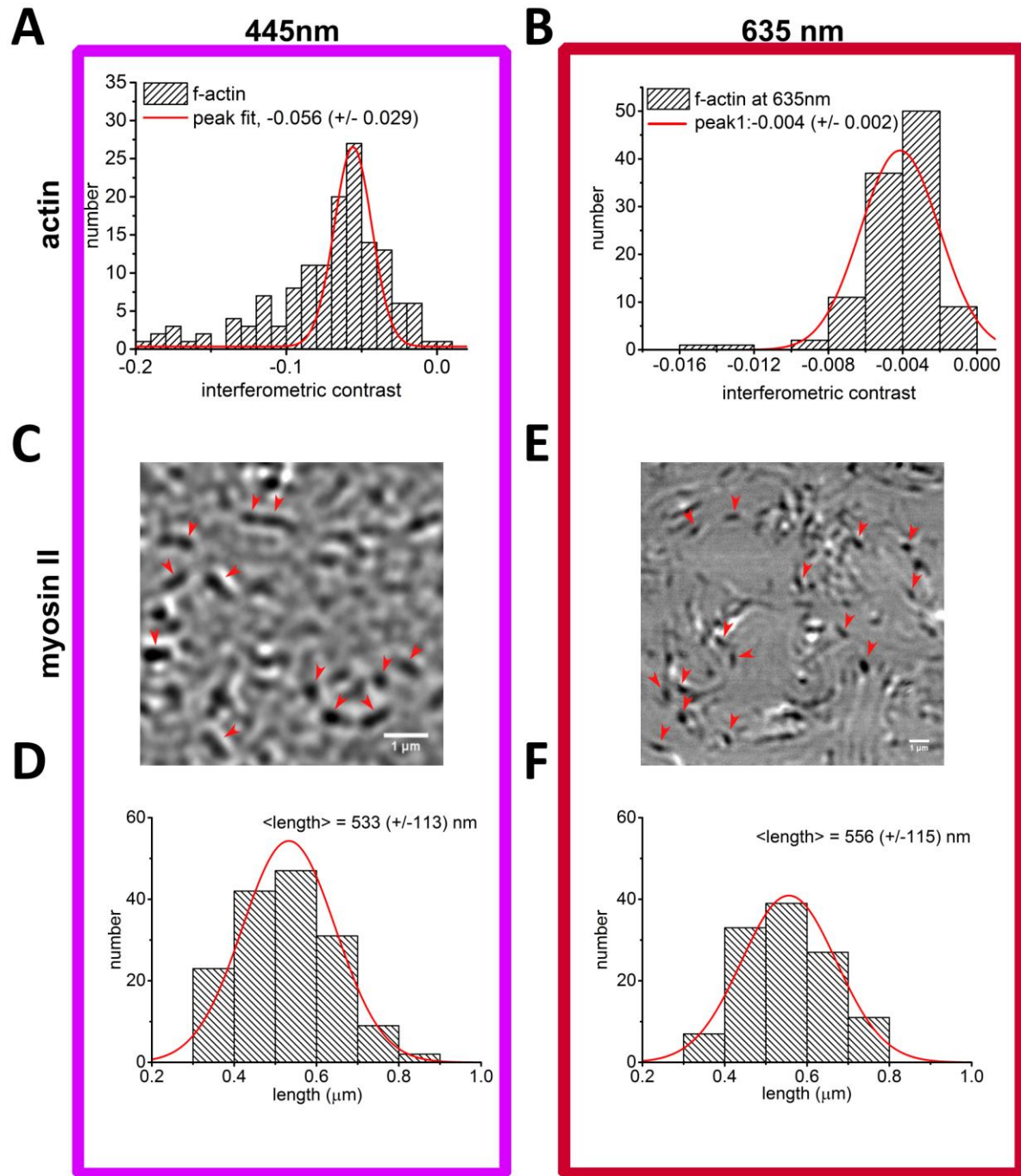


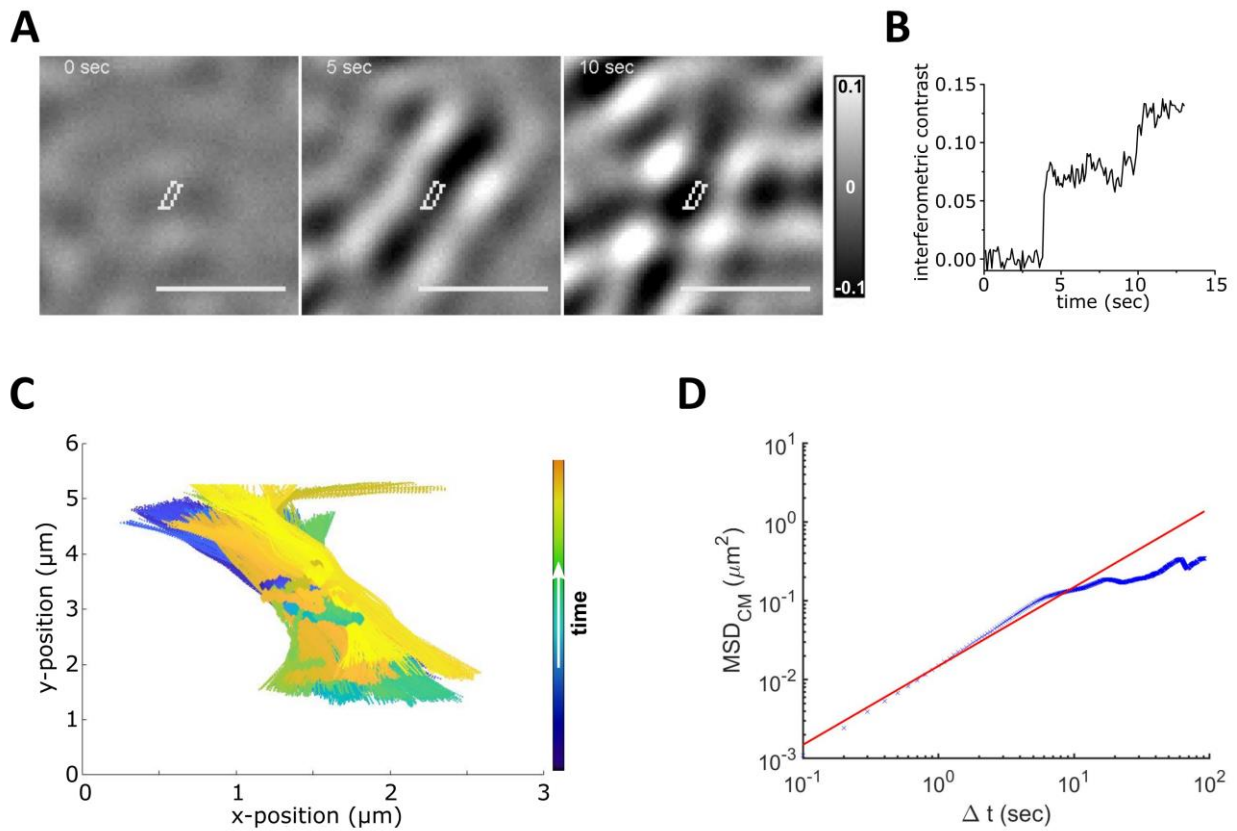
Figure 4



Sup Figure 1

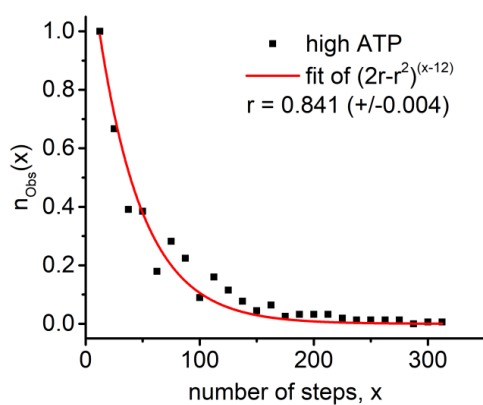


Sup Figure 2



Sup Fig3

A



B

